THE JOURNAL OF PHYSICAL CHEMISTRY Letters

pubs.acs.org/JPCL Letter

Direct Identification of Mixed-Metal Centers in Metal–Organic Frameworks: $Cu_3(BTC)_2$ Transmetalated with Rh^{2+} Ions

Kamolrat Metavarayuth, Otega Ejegbavwo, Gavin McCarver, Michael L. Myrick, Thomas M. Makris, Konstantinos D. Vogiatzis, Sanjaya D. Senanayake, Olivia M. Manley, Amani M. Ebrahim, Anatoly I. Frenkel, Sooyeon Hwang, Thayalan Rajeshkumar, Juan D. Jimenez, Kexun Chen, Natalia B. Shustova,* and Donna A. Chen*

Cite This: J. Phys. Chem. Lett. 2020, 11, 8138–8144

ABSTRACT: Raman spectroscopy was used to establish direct evidence of heterometallic metal centers in a metal–organic framework (MOF). The $Cu_3(BTC)_2$ MOF HKUST-1 (BTC^{3-} = benzenetricarboxylate) was transmetalated by heating it in a solution of $RhCl_3$ to substitute Rh^{2+} ions for Cu^{2+} ions in the dinuclear paddlewheel nodes of the framework. In addition to the Cu–Cu and Rh–Rh stretching modes, Raman spectra of $(Cu_xRh_{1-x})_3(BTC)_2$ show the Cu–Rh stretching mode, indicating that mixed-metal Cu–Rh nodes are formed after transmetalation. Density functional theory studies confirmed the assignment of a Raman peak at 285 cm^{-1} to the Cu–Rh stretching vibration. Electron paramagnetic resonance spectroscopy experiments further supported the conclusion that Rh^{2+} ions are substituted into the paddlewheel nodes of $Cu_3(BTC)_2$ to form an isostructural heterometallic MOF, and electron microscopy studies showed that Rh and Cu are homogeneously distributed in $(Cu_xRh_{1-x})_3(BTC)_2$ on the nanoscale.

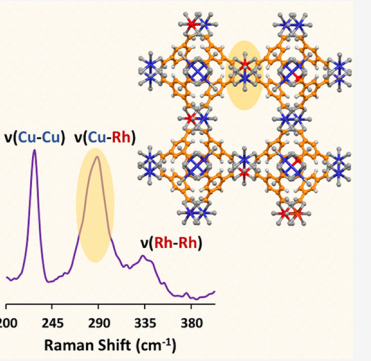

Metal–organic frameworks (MOFs) are crystalline hybrid inorganic–organic materials with remarkable synthetic tunability in terms of the geometry and composition of the metal centers, the nature of the organic linkers, and the pore sizes.[1−5] MOFs have found numerous applications in gas separations and storage[6−9] as well as in liquid-phase catalysis[5,10−14] and have also served as materials for electronic devices and sensors.[15−17] Furthermore, heterometallic MOFs have attracted attention because of their unique catalytic[2,5,18−20] and electronic properties.[3,21,22] Recently our group demonstrated the first gas-phase catalytic process occurring at the metal nodes of a crystalline MOF.[23] Specifically, $(Cu_xRh_{1-x})_3(BTC)_2$ (abbreviated CuRhBTC) was active for the hydrogenation of propylene to propane, with the Rh^{2+} ions in the framework serving as the catalytically active sites. CuRhBTC was synthesized by transmetalation of monometallic $Cu_3(BTC)_2$ (HKUST-1, abbreviated CuBTC) upon heating in a solution of $RhCl_3$. The proposed mechanism for propylene hydrogenation on the CuRhBTC catalyst is based on the assumption that some fraction of Cu^{2+} ions are replaced by Rh^{2+} ions in the paddlewheel nodes of the MOF.[23] To date, however, there have been no definitive reports in the literature proving that the rhodium cations are incorporated into the paddlewheel nodes in CuRhBTC, and therefore a number of different experimental techniques were employed to address this issue.

In this work, we report that Raman spectroscopy and density functional theory (DFT) calculations were used to identify Cu–Rh stretching vibrations in CuRhBTC; this conclusively demonstrates that Rh^{2+} ions are integrated into the paddlewheel nodes of the MOF, and that heterometallic nodes coexist with pure Cu and pure Rh nodes for Rh concentrations of ∼20–30%. Solid-state electron paramagnetic resonance (EPR) spectroscopy investigations further support the presence of mixed Cu–Rh nodes in CuRhBTC. Scanning transmission electron microscopy (STEM) studies with energy-dispersive X-ray spectroscopy (EDX) elemental mapping show that the copper and rhodium cations are uniformly dispersed throughout the MOF on the nanometer scale.

Raman spectroscopy experiments were conducted to potentially identify vibrations associated with the Cu–Rh stretches in the paddlewheel node. Before all experiments, the MOFs were activated by heating in vacuo to remove coordinating solvent or water molecules, as described in Methods. The Raman spectra of CuBTC, CuRhBTC, and RhBTC collected at an excitation wavelength of 532 nm are shown in Figure 1, with the major peak assignments based on reports in the literature for the monometallic MOFs.[24−26]

Received: August 19, 2020
Accepted: September 7, 2020
Published: September 7, 2020

https://dx.doi.org/10.1021/acs.jpclett.0c02539
J. Phys. Chem. Lett. 2020, 11, 8138–8144

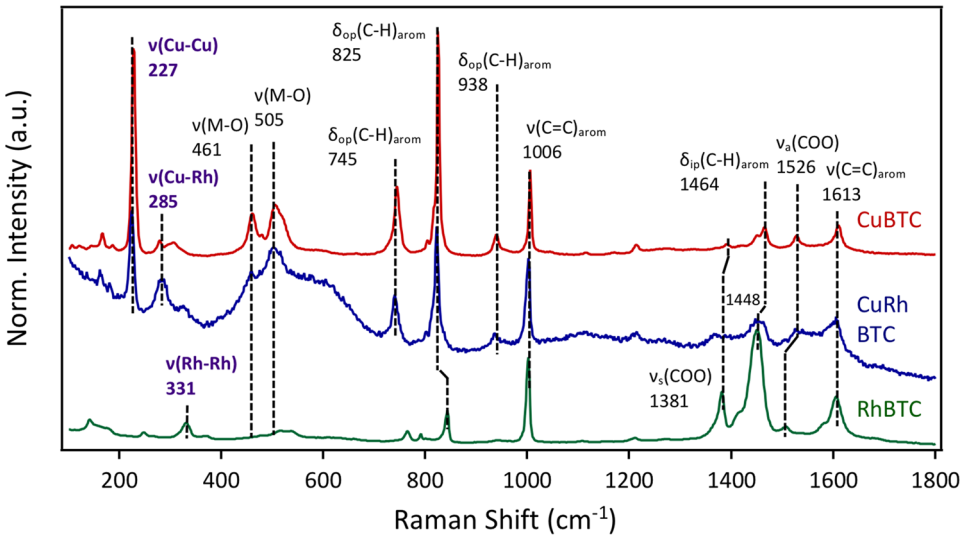

Figure 1. Raman spectra at 532 nm for CuBTC (red), CuRhBTC with 21% Rh (blue), and RhBTC (green). Peak positions are given in cm^{-1}, and the intensities are normalized to that of the 1006 cm^{-1} peak of CuBTC. Ligand vibrational modes at 1381 and 1448 cm^{-1} mix the symmetric COO carboxylate motion with the degenerate in-plane bending mode of the aromatic C−H groups.[25]

Since the peaks for the metal−metal modes all appear below 800 cm^{-1}, they are the focus of Figure 2, which shows Raman

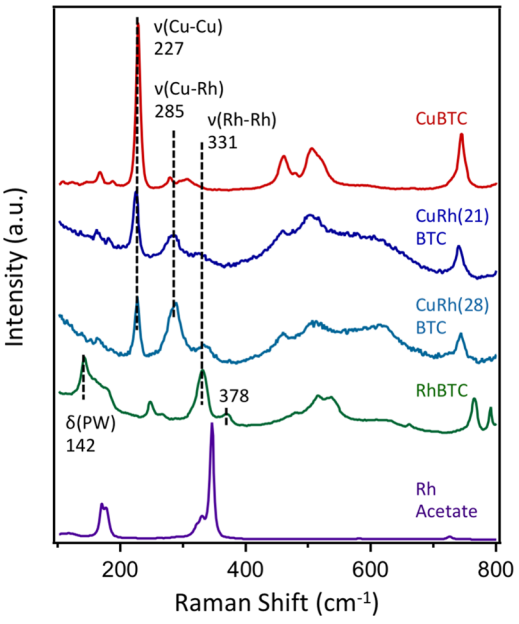

Figure 2. Raman spectra at 532 nm for CuBTC (red, ×0.5), CuRhBTC with 21% Rh (dark blue, ×5), CuRhBTC with 28% Rh (light blue, ×5), RhBTC (green), and rhodium(II) acetate (purple, ×0.05).

spectra of CuRhBTC at two different Rh concentrations (21% and 28%) along with those of CuBTC, RhBTC, and rhodium(II) acetate. The intense peak at 227 cm^{-1} in the spectrum of CuBTC is attributed to the Cu−Cu stretch for activated CuBTC and is consistent with previous Raman studies.[24,26−28] This peak also has high intensity at an excitation wavelength of 638 nm, but its relative intensity is much lower with excitation at 473 nm (Figure S1). The fact that the CuBTC, CuRhBTC, and RhBTC MOFs have distinctly different colors (blue, deep blue, and dark green, respectively; Figure S2) suggests strong resonance enhancement at specific wavelengths in the visible region. For RhBTC, the ν(Cu−Cu) peak at 227 cm^{-1} is absent, and the peaks at 331 and 142 cm^{-1} are attributed to the Rh−Rh stretch and a Rh−Rh paddlewheel deformation, respectively.[25] In comparison, the Raman spectrum of rhodium(II) acetate exhibits peaks at 330 and 346 cm^{-1} assigned to Rh−Rh stretching vibrations that are in the same wavenumber range as those assigned here for RhBTC. For CuRhBTC with ∼20% Rh, a pronounced feature at 285 cm^{-1} is detected in addition to the ν(Cu−Cu) and ν(Rh−Rh) modes. This 285 cm^{-1} peak is attributed to a Cu−Rh vibration and increases in intensity as the concentration of Rh in CuRhBTC is increased to ∼30%.

DFT Raman calculations for the molecular model with a Cu−Rh paddlewheel predict that the ν(Cu−Rh) mode should appear at 300 cm^{-1}, which is in agreement with the value of 285 cm^{-1} from experiments. Moreover, DFT calculations for molecular models with the Cu−Cu and Rh−Rh paddlewheel structures predict the Cu−Cu stretch occurs at 242 cm^{-1} and the Rh−Rh stretch occurs at 357 cm^{-1}. These values are within 15−26 cm^{-1} of the experimental measurements (227 and 331 cm^{-1}, respectively) and are also consistent with the stretching frequencies reported in the literature for CuBTC[24] and RhBTC.[25]

Furthermore, time-dependent DFT (TDDFT) calculations confirm that the high intensity of the Cu−Cu stretch relative to the Cu−Rh and Rh−Rh stretches in the Raman spectra can be attributed to resonance enhancement, given that electronic excitation results in structural changes that can contribute to the enhancement of Raman scattering.[29] Four d to σ^* excited states were identified for the antiferromagnetically coupled singlet of the CuBTC node with energies corresponding to the 532 nm excitation wavelength (Figure S3), whereas no excitations were observed close to the same energy for the CuRhBTC and RhBTC nodes. The excitation of the CuBTC node is found to cause an increase in the Cu−Cu distance by 11.8% relative to the ground state (2.75 vs 2.46 Å), and this distortion is the likely source of the observed resonance enhancement of the Cu−Cu stretching mode.

Notably, CuBTC does not have a formal bond between the Cu ions, but there is a Cu−Cu stretching vibration that occurs

https://dx.doi.org/10.1021/acs.jpclett.0c02539
J. Phys. Chem. Lett. 2020, 11, 8138−8144

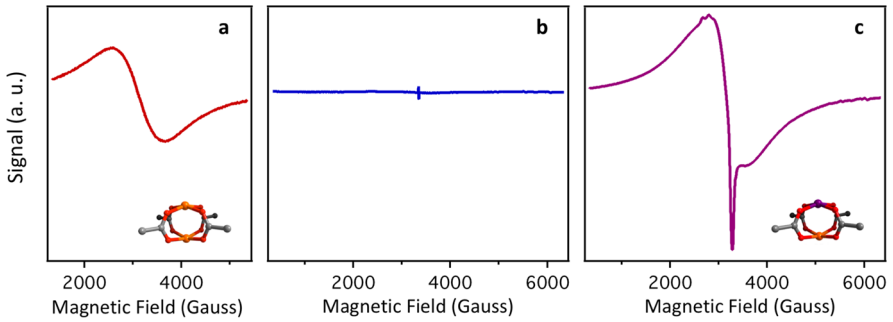

Figure 3. EPR spectra of (a) CuBTC, (b) rhodium(II) acetate, and (c) CuRhBTC. The monometallic and heterometallic paddlewheel structures are shown in (a) and (c).

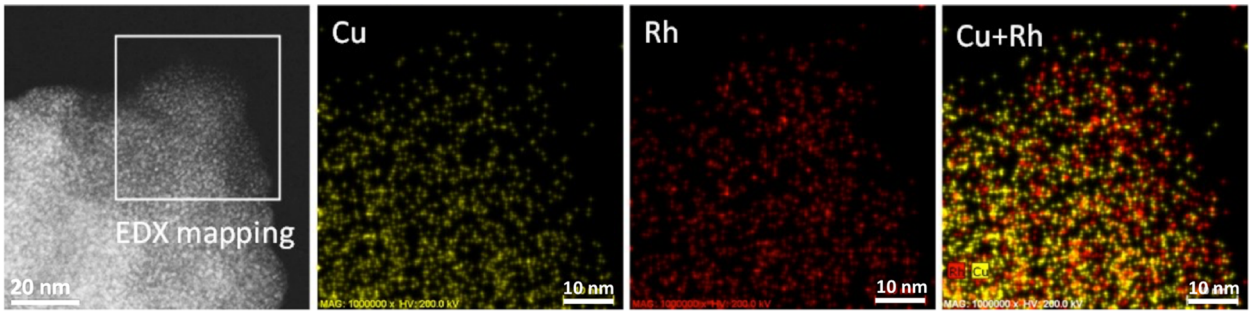

Figure 4. (left) HAADF-STEM image of the CuRhBTC MOF drop-cast onto a TEM grid. (middle) STEM-EDX elemental maps for Cu and Rh and (right) their overlay.

through the associated ligands. Similarly, the ν(Cu−Rh) mode does not necessarily involve a true covalent bond between the metal centers. In conclusion, the Raman data for CuRhBTC demonstrate clear evidence that Rh^{2+} ions must be incorporated into the paddlewheel node in order for the associated ν(Cu−Rh) vibrations to be observed.

Solid-state EPR investigations further supports the presence of mixed-metal paddlewheel nodes in CuRhBTC. EPR measurements were carried out for CuBTC, CuRhBTC, and rhodium(II) acetate as a crystalline standard for the dirhodium paddlewheel. As shown in Figure 3a, the spectrum of CuBTC displays an extremely broad isotropic signal centered at g = 2.17, which is consistent with room-temperature EPR spectra of CuBTC previously reported in the literature.[30−32] CuBTC[30,31] and other structures with the dicopper paddlewheel motif[33−36] are known to have an antiferromagnetically coupled singlet ground state and a ferromagnetic excited triplet state that is ∼30 meV[37] higher in energy. At lower temperatures (<90 K), CuBTC is EPR-silent due to the S = 0 ground state, but at temperatures of ∼100 K, the active S = 1 triplet state is populated.[31] The broad EPR spectrum for CuBTC at room temperature is therefore attributed to spin exchange between the Cu^{2+} paddlewheels via the BTC linkers, resulting in averaging of the anisotropic spectral features from individual Cu dimers.[30−32] Rh^{2+} exists as a d^7 ion in rhodium(II) acetate, which is diamagnetic due to the formation of Rh−Rh bonds and resultant spin coupling.[38] As expected, Rh^{2+} is essentially EPR-silent, with a very small peak at g = 2.00 appearing most likely from trace magnetic impurities. The EPR signal of CuRhBTC could present two possibilities: antiferromagnetically coupled Cu^{2+}−Rh^{2+} would have S = 0 and thus would be EPR-silent, or the signal of mononuclear Cu would be apparent if the species are not magnetically coupled. The spectrum of CuRhBTC shows a broad signal associated with some remaining CuBTC but also shows a new sharp signal centered at g = 2.13. This new peak for CuRhBTC is attributed to mononuclear Cu^{2+} and also displays the hyperfine splitting pattern that is typically associated with the mononuclear species.[30,35] Therefore, some of the copper cations in the paddlewheel nodes must be substituted with rhodium cations to produce magnetically isolated copper sites.

Electron microscopy studies demonstrate that the spatial distribution of Cu^{2+} and Rh^{2+} ions in CuRhBTC is uniform on the nanometer scale. Figure 4 shows a high-angle annular dark-field scanning transmission electron microscopy (HAADF-STEM) image of CuRhBTC, and elemental mapping by STEM-EDX indicates that the copper and rhodium cations are distributed throughout the CuRhBTC MOF in a homogeneous manner. Furthermore, scanning electron microscopy (SEM) images on a larger scale (micrometers) illustrate that CuBTC exists as large faceted crystals while CuRhBTC is composed of smaller crystallites with less well defined facets (Figure S4), and RhBTC consists of even smaller crystallites with no distinct facets (Figure S5). EDX elemental maps for the SEM images also exhibit relatively uniform spatial distributions for the copper and rhodium in CuRhBTC on this larger size scale (Figure S6).

In summary, Raman spectroscopy has been used to identify Cu−Rh mixed-metal centers in the CuRhBTC MOF on the basis of the ν(Cu−Rh) mode, which appears at 285 cm^{-1}. For CuRhBTC with Rh concentrations of 20−30%, ν(Cu−Cu) and ν(Rh−Rh) vibrational modes can also be observed although the latter is rare for the lower 20% Rh concentration. DFT calculations for a molecular model containing the Cu−Rh paddlewheel center confirm the assignment of the Cu−Rh stretch. Solid-state EPR studies further support the presence of Cu−Rh nodes since distinctive features of mononuclear Cu

https://dx.doi.org/10.1021/acs.jpclett.0c02539
J. Phys. Chem. Lett. 2020, 11, 8138−8144

ions are observed. On the basis of the uniform spatial distributions for Cu and Rh ions on the nano- and micrometer scales for CuRhBTC, it is reasonable to expect a statistical distribution of Rh^{2+} in the paddlewheel nodes. Specifically, for a Rh concentration of 20%, 32% of the nodes should be Cu−Rh, 4% should be Rh−Rh, and 64% should be Cu−Cu. Given the unique electronic and chemical properties reported for MOFs with heterometallic nodes, Raman spectroscopy can serve as a valuable tool for identifying these mixed-metal centers.

METHODS

Experimental Methods. CuBTC,[39] CuRhBTC,[23] and RhBTC[25] were synthesized by previously reported procedures. The powder X-ray diffraction patterns for these MOFs demonstrate that monometallic CuBTC and heterometallic CuRhBTC are highly crystalline and isostructural (Figure S7).[40] RhBTC is less crystalline than CuBTC and CuRhBTC based on the greater full width at half-maximum for the RhBTC peaks (Figure S7), and this result is in agreement with other studies reporting the difficulty of preparing crystalline RhBTC.[25,41] The concentration of Rh in the CuRhBTC was established by inductively coupled plasma mass spectrometry after the MOF was digested in acidic solution.[23] Before Raman, EPR, and electron microscopy experiments, the Rh-containing MOFs were activated by heating at 100 °C for 24 h in vacuo, whereas the CuBTC sample was activated by heating at 160 °C for 48 h in vacuo. This activation process removes solvent and water molecules adsorbed at the undercoordinated metal sites as well as adsorbates from the pores of the MOFs. Rhodium(II) acetate (99.99%) was purchased from Sigma-Aldrich and used as received.

Raman spectra at an excitation wavelength of 532 nm were acquired on a Horiba LabRAM HR Evolution VIS+NIR Raman microscope equipped with a UP-ULF-532-HREV ultralow frequency kit (minimum usable Raman shift ∼10 cm^{-1}). Excitation was performed with 1% of a measured maximum excitation power of 78 mW; the laser power was set to avoid damage to the sample, and all of the samples were examined for damage after measurement. The Raman aperture was set to 100 μm with a ruled 600 lines/mm grating blazed at a wavelength of 500 nm, providing a nominal resolution of 3.5 cm^{-1}. The detector for this instrument was a standard Horiba Syncerity OE 1024 × 256 pixel thermoelectrically cooled charge-coupled device (CCD) provided with the LabRAM instrument. Each individual spectrum was the result of 60 s of integration summed over 10 acquisition cycles for a total measurement time of 600 s. The 638 and 473 nm laser measurements were carried out on a Horiba X-Plora Plus instrument using a slit width of 100 μm, a hole size of 500 μm, and a grating of 1200 lines/mm equipped with a thermoelectric cooled CCD detector. Additional experimental details are provided in the Supporting Information.

For the solid-state EPR experiments, CuBTC, CuRhBTC, and rhodium(II) acetate powders were placed into quartz tubes, and the EPR spectra were collected using a Bruker X-band EMXplus EPR spectrometer at room temperature with a modulation amplitude of 10 mT and a microwave power of 1 mW. The reported spectra are averages of five scans. The CuBTC and CuRhBTC samples were activated by heating in vacuo immediately before the experiment as described above.

HAADF-STEM images and STEM-EDX elemental maps were collected using an aberration-corrected cold field-emission gun on a Hitachi HD 2700C scanning transmission electron microscope equipped with a Bruker SSD EDX detector operating at an accelerating voltage of 200 kV. This electron microscope was located at the Center for Functional Nanomaterials at Brookhaven National Laboratory. Samples were brushed onto a silicon nitride TEM window grid (SiMpore Inc.) or drop-cast from a suspension of the MOF in ethanol. High-resolution SEM images and SEM-EDX elemental maps were collected using a JEOL JSM 7600F thermal field-emission scanning electron microscope at the Center for Functional Nanomaterials at Brookhaven National Laboratory. The samples were brushed onto carbon tape and Au-sputtered to create a 10 nm Au conductive surface. The micrographs were acquired at a working distance of 7.5 mm at 20 kV.

Computational Methods. All of the calculations were performed with the ORCA 4.2 software package. The PBE[42] and B3LYP[43−45] density functionals were utilized since they have been shown to be reliable for such spectroscopic studies. For the transition metals, the def2-TZVPP basis set was used (with the corresponding effective core potential for Rh), while the def2-TZVP[46] basis set was used for all other atoms. Tight convergence criteria were employed for both the SCF cycles and geometric optimization steps. Grimme's D3 semiempirical correction[47] was included with the Becke−Johnson damping function[48−50] together with the resolution of identity approximation to accelerate the computation of the four-index integrals.[51] All of the Raman spectra were computed numerically with the harmonic approximation, and each mode was corrected by an empirical scaling factor of 1.0306.[52] A truncated molecular model was used that consisted of a dimer paddlewheel structure capped with the benzenetricarboxylate linker, and acidic hydrogens were replaced with lithium cations to best retain the rigidity of the MOF and to better approximate the neighboring dinuclear nodes (Figure S8a). The ground spin states of the nodes considered in this study are a closed-shell singlet for the RhBTC complex, an antiferromagnetically coupled singlet for CuBTC, and a triplet for CuRhBTC. TDDFT calculations were performed in order to elucidate the electronic structure of the CuBTC node in the Raman experiments. The CAM-B3LYP density functional[53] and a smaller molecular model consisting of the paddlewheel node capped with acetate groups (Figure S8b) were used to calculate the excited states of the CuBTC structure around 18 800 cm^{-1}, which corresponds to the excitation wavelength of 532 nm.

ASSOCIATED CONTENT

Supporting Information

The Supporting Information is available free of charge at https://pubs.acs.org/doi/10.1021/acs.jpclett.0c02539.

Raman spectra of MOFs collected with excitation at 638 and 473 nm; photographs of activated MOFs showing their colors; orbitals involved in the excitation of the CuBTC nodes; SEM images of CuBTC and CuRhBTC; HAADF-STEM image of RhBTC with EDX elemental maps; SEM image of CuRhBTC with EDX elemental maps; PXRD data for CuBTC, CuRhBTC, and RhBTC; molecular models of the paddlewheel structures; and description of the Raman experiments (PDF)

https://dx.doi.org/10.1021/acs.jpclett.0c02539
J. Phys. Chem. Lett. 2020, 11, 8138−8144

AUTHOR INFORMATION

Corresponding Authors

Donna A. Chen − *Department of Chemistry and Biochemistry, University of South Carolina, Columbia, South Carolina 29208, United States;* orcid.org/0000-0003-4962-5530; Phone: 803-777-1050; Email: dachen@sc.edu; Fax: 803-777-9521

Natalia B. Shustova − *Department of Chemistry and Biochemistry, University of South Carolina, Columbia, South Carolina 29208, United States;* orcid.org/0000-0003-3952-1949; Email: shustova@sc.edu

Authors

Kamolrat Metavarayuth − *Department of Chemistry and Biochemistry, University of South Carolina, Columbia, South Carolina 29208, United States*

Otega Ejegbavwo − *Department of Chemistry and Biochemistry, University of South Carolina, Columbia, South Carolina 29208, United States*

Gavin McCarver − *Department of Chemistry, University of Tennessee Knoxville, Knoxville, Tennessee 37996, United States*

Michael L. Myrick − *Department of Chemistry and Biochemistry, University of South Carolina, Columbia, South Carolina 29208, United States;* orcid.org/0000-0002-6905-0925

Thomas M. Makris − *Department of Chemistry and Biochemistry, University of South Carolina, Columbia, South Carolina 29208, United States;* orcid.org/0000-0001-7927-620X

Konstantinos D. Vogiatzis − *Department of Chemistry, University of Tennessee Knoxville, Knoxville, Tennessee 37996, United States;* orcid.org/0000-0002-7439-3850

Sanjaya D. Senanayake − *Chemistry Division, Brookhaven National Laboratory, Upton, New York 11973, United States;* orcid.org/0000-0003-3991-4232

Olivia M. Manley − *Department of Chemistry and Biochemistry, University of South Carolina, Columbia, South Carolina 29208, United States*

Amani M. Ebrahim − *Department of Materials Science and Chemical Engineering, Stony Brook University, Stony Brook, New York 11794, United States;* orcid.org/0000-0001-9979-2586

Anatoly I. Frenkel − *Chemistry Division, Brookhaven National Laboratory, Upton, New York 11973, United States; Department of Materials Science and Chemical Engineering, Stony Brook University, Stony Brook, New York 11794, United States;* orcid.org/0000-0002-5451-1207

Sooyeon Hwang − *Center for Functional Nanomaterials, Brookhaven National Laboratory, Upton, New York 11973, United States;* orcid.org/0000-0001-5606-6728

Thayalan Rajeshkumar − *Department of Chemistry, University of Tennessee Knoxville, Knoxville, Tennessee 37996, United States*

Juan D. Jimenez − *Department of Chemical Engineering, University of South Carolina, Columbia, South Carolina 29208, United States*

Kexun Chen − *Department of Chemistry and Biochemistry, University of South Carolina, Columbia, South Carolina 29208, United States*

Complete contact information is available at: https://pubs.acs.org/10.1021/acs.jpclett.0c02539

Notes

The authors declare no competing financial interest.

ACKNOWLEDGMENTS

This research was supported by the U.S. Department of Energy, Office of Science, Office of Basic Energy Sciences (DOE-BES) under Award DE-SC0019360. In addition, the University of South Carolina's Advance Support for Innovative Research Excellence program is acknowledged for funding preliminary studies. N.B.S. acknowledges the support of the Sloan Fellowship provided by the Alfred P. Sloan Foundation and the Camille Dreyfus Teacher-Scholar Award provided by the Dreyfus Foundation. STEM and SEM analyses by A.M.E and A.I.F. discussed here were supported as part of the Catalysis Center for Energy Innovation, an Energy Frontier Research Center funded by DOE-BES under Award DE-SC0001004. We also acknowledge the Center for Functional Nanomaterials, a U.S. DOE Office of Science Facility at Brookhaven National Laboratory under Contract DE-SC0012704.

REFERENCES

(1) Furukawa, H.; Cordova, K. E.; O'Keeffe, M.; Yaghi, O. M. The Chemistry and Applications of Metal−Organic Frameworks. *Science* **2013**, *341*, 1230444.

(2) Yuan, S.; Qin, J.-S.; Li, J.; Huang, L.; Feng, L.; Fang, Y.; Lollar, C.; Pang, J.; Zhang, L.; Sun, D.; Alsalme, A.; Cagin, T.; Zhou, H.-C. Retrosynthesis of Multi-Component Metal−Organic Frameworks. *Nat. Commun.* **2018**, *9*, 808.

(3) Islamoglu, T.; Goswami, S.; Li, Z. Y.; Howarth, A. J.; Farha, O. K.; Hupp, J. T. Postsynthetic Tuning of Metal−Organic Frameworks for Targeted Applications. *Acc. Chem. Res.* **2017**, *50*, 805−13.

(4) Huang, N.; Wang, K. C.; Drake, H.; Cai, P. Y.; Pang, J. D.; Li, J. L.; Che, S.; Huang, L.; Wang, Q.; Zhou, H. C. Tailor-Made Pyrazolide-Based Metal−Organic Frameworks for Selective Catalysis. *J. Am. Chem. Soc.* **2018**, *140*, 6383−90.

(5) Drake, T.; Ji, P. F.; Lin, W. B. Site Isolation in Metal−Organic Frameworks Enables Novel Transition Metal Catalysis. *Acc. Chem. Res.* **2018**, *51*, 2129−38.

(6) He, Y. B.; Zhou, W.; Qian, G. D.; Chen, B. L. Methane Storage in Metal−Organic Frameworks. *Chem. Soc. Rev.* **2014**, *43*, 5657−78.

(7) Herm, Z. R.; Bloch, E. D.; Long, J. R. Hydrocarbon Separations in Metal−Organic Frameworks. *Chem. Mater.* **2014**, *26*, 323−38.

(8) Li, J. R.; Sculley, J.; Zhou, H. C. Metal−Organic Frameworks for Separations. *Chem. Rev.* **2012**, *112*, 869−932.

(9) Phan, A.; Doonan, C. J.; Uribe-Romo, F. J.; Knobler, C. B.; O'Keeffe, M.; Yaghi, O. M. Synthesis, Structure, and Carbon Dioxide Capture Properties of Zeolitic Imidazolate Frameworks. *Acc. Chem. Res.* **2010**, *43*, 58−67.

(10) Lee, J.; Farha, O. K.; Roberts, J.; Scheidt, K. A.; Nguyen, S. T.; Hupp, J. T. Metal−Organic Framework Materials as Catalysts. *Chem. Soc. Rev.* **2009**, *38*, 1450−9.

(11) Chughtai, A. H.; Ahmad, N.; Younus, H. A.; Laypkov, A.; Verpoort, F. Metal−Organic Frameworks: Versatile Heterogeneous Catalysts for Efficient Catalytic Organic Transformations. *Chem. Soc. Rev.* **2015**, *44*, 6804−49.

(12) Liu, J. W.; Chen, L. F.; Cui, H.; Zhang, J. Y.; Zhang, L.; Su, C. Y. Applications of Metal−Organic Frameworks in Heterogeneous Supramolecular Catalysis. *Chem. Soc. Rev.* **2014**, *43*, 6011−61.

(13) Gascon, J.; Corma, A.; Kapteijn, F.; Llabrés i Xamena, F. X. Metal Organic Framework Catalysis: *Quo vadis*? *ACS Catal.* **2014**, *4*, 361−78.

(14) Jiao, L.; Wang, Y.; Jiang, H. L.; Xu, Q. Metal−Organic Frameworks as Platforms for Catalytic Applications. *Adv. Mater.* **2018**, *30*, 1703663.

(15) Kreno, L. E.; Leong, K.; Farha, O. K.; Allendorf, M.; Van Duyne, R. P.; Hupp, J. T. Metal−Organic Framework Materials as Chemical Sensors. *Chem. Rev.* **2012**, *112*, 1105−25.
(16) Stavila, V.; Talin, A. A.; Allendorf, M. D. MOF-Based Electronic and Optoelectronic Devices. *Chem. Soc. Rev.* **2014**, *43*, 5994−6010.
(17) Stassen, I.; Burtch, N.; Talin, A.; Falcaro, P.; Allendorf, M.; Ameloot, R. An Updated Roadmap for the Integration of Metal−Organic Frameworks with Electronic Devices and Chemical Sensors. *Chem. Soc. Rev.* **2017**, *46*, 3185−241.
(18) Huang, Y. B.; Liang, J.; Wang, X. S.; Cao, R. Multifunctional Metal−Organic Framework Catalysts: Synergistic Catalysis and Tandem Reactions. *Chem. Soc. Rev.* **2017**, *46*, 126−57.
(19) Zheng, F. Q.; Xiang, D.; Li, P.; Zhang, Z. W.; Du, C.; Zhuang, Z. H.; Li, X. K.; Chen, W. Highly Conductive Bimetallic Ni−Fe Metal Organic Framework as a Novel Electrocatalyst for Water Oxidation. *ACS Sustainable Chem. Eng.* **2019**, *7*, 9743−9.
(20) Brozek, C. K.; Dinca, M. Ti^{3+}-, $V^{2+/3+}$-, $Cr^{2+/3+}$-, Mn^{2+}-, and Fe^{2+}-Substituted MOF-5 and Redox Reactivity in Cr- and Fe-MOF-5. *J. Am. Chem. Soc.* **2013**, *135*, 12886−91.
(21) Dolgopolova, E. A.; Brandt, A. J.; Ejegbavwo, O. A.; Duke, A. S.; Maddumapatabandi, T. D.; Galhenage, R. P.; Larson, B. W.; Reid, O. G.; Ammal, S. C.; Heyden, A.; Chandrashekhar, M.; Stavila, V.; Chen, D. A.; Shustova, N. B. Electronic Properties of Bimetallic Metal−Organic Frameworks (MOFs): Tailoring the Density of Electronic States through MOF Modularity. *J. Am. Chem. Soc.* **2017**, *139*, 5201−9.
(22) Kobayashi, Y.; Jacobs, B.; Allendorf, M. D.; Long, J. R. Conductivity, Doping, and Redox Chemistry of a Microporous Dithiolene-Based Metal−Organic Framework. *Chem. Mater.* **2010**, *22*, 4120−2.
(23) Shakya, D. M.; Ejegbavwo, O. A.; Rajeshkumar, T.; Senanayake, S. D.; Brandt, A. J.; Farzandh, S.; Acharya, N.; Ebrahim, A. M.; Frenkel, A. I.; Rui, N.; Tate, G. L.; Monnier, J. R.; Vogiatzis, K. D.; Shustova, N. B.; Chen, D. A. Selective Catalytic Chemistry at Rhodium(II) Nodes in Bimetallic Metal−Organic Frameworks. *Angew. Chem., Int. Ed.* **2019**, *58*, 16533−7.
(24) Todaro, M.; Alessi, A.; Sciortino, L.; Agnello, S.; Cannas, M.; Gelardi, F. M.; Buscarino, G. Investigation by Raman Spectroscopy of the Decomposition Process of HKUST-1 Upon Exposure to Air. *J. Spectrosc.* **2016**, *2016*, 8074297.
(25) Heinz, W. R.; Kratky, T.; Drees, M.; Wimmer, A.; Tomanec, O.; Gunther, S.; Schuster, M.; Fischer, R. A. Mixed Precious-Group Metal−Organic Frameworks: a Case Study of the HKUST-1 Analogue $Ru_xRh_{3-x}(BTC)_2$. *Dalton Trans* **2019**, *48*, 12031−9.
(26) Prestipino, C.; Regli, L.; Vitillo, J. G.; Bonino, F.; Damin, A.; Lamberti, C.; Zecchina, A.; Solari, P. L.; Kongshaug, K. O.; Bordiga, S. Local Structure of Framework Cu(II) in HKUST-1 Metallorganic Framework: Spectroscopic Characterization Upon Activation and Interaction with Adsorbates. *Chem. Mater.* **2006**, *18*, 1337−46.
(27) Kim, H. K.; Yun, W. S.; Kim, M. B.; Kim, J. Y.; Bae, Y. S.; Lee, J.; Jeong, N. C. A Chemical Route to Activation of Open Metal Sites in the Copper-Based Metal−Organic Framework Materials HKUST-1 and Cu-MOF-2. *J. Am. Chem. Soc.* **2015**, *137*, 10009−15.
(28) Song, H. I.; Bae, J.; Lee, E. L.; Kirlikovali, K. O.; Farha, O. K.; Jeong, N. C. Vibrational Paddlewheel Cu-Cu Node in Metal−Organic Frameworks: Probe of Nonradiative Relaxation. *J. Phys. Chem. C* **2020**, *124*, 13187−95.
(29) Hirakawa, A. Y.; Tsuboi, M. Molecular Geometry in an Excited Electronic State and A Preresonance Raman Effect. *Science* **1975**, *188*, 359−61.
(30) Todaro, M.; Buscarino, G.; Sciortino, L.; Alessi, A.; Messina, F.; Taddei, M.; Ranocchiari, M.; Cannas, M.; Gelardi, F. M. Decomposition Process of Carboxylate MOF HKUST-1 Unveiled at the Atomic Scale Level. *J. Phys. Chem. C* **2016**, *120*, 12879−89.
(31) Poppl, A.; Kunz, S.; Himsl, D.; Hartmann, M. CW and Pulsed ESR Spectroscopy of Cupric Ions in the Metal−Organic Framework Compound $Cu_3(BTC)_2$. *J. Phys. Chem. C* **2008**, *112*, 2678−84.
(32) Bohlmann, W.; Poppl, A.; Sabo, M.; Kaskel, S. Characterization of the Metal−Organic Framework Compound Cu_3(Benzene 1,3,5-Tricarboxylate)$_2$ by Means of Xe-129 Nuclear Magnetic and Electron Paramagnetic Resonance Spectroscopy. *J. Phys. Chem. B* **2006**, *110*, 20177−81.
(33) Bleaney, B.; Bowers, K. D. Anomalous Paramagnetism of Copper Acetate. *Proc. R. Soc. London, Ser. A* **1952**, *214*, 451−65.
(34) Zhaobin, W.; Qin, X.; Xiexian, G.; Grange, P.; Delmon, B. Titania-Modified Hydrodesulfurization Catalysts: II. Dispersion State and Catalytic Activity of Molybdena Supported on Titania-Alumina Carrier. *Appl. Catal.* **1991**, *75*, 179−91.
(35) Simenas, M.; Kobalz, M.; Mendt, M.; Eckold, P.; Krautscheid, H.; Banys, J.; Poppl, A. Synthesis, Structure, and Electron Paramagnetic Resonance Study of a Mixed Valent Metal−Organic Framework Containing Cu_2 Paddle-Wheel Units. *J. Phys. Chem. C* **2015**, *119*, 4898−907.
(36) Zhang, X. X.; Chui, S. S. Y.; Williams, I. D. Cooperative Magnetic Behavior in the Coordination Polymers $Cu_3(TMA)_2L_3$ (L = H_2O, Pyridine). *J. Appl. Phys.* **2000**, *87*, 6007−9.
(37) Hendon, C. H.; Walsh, A. Chemical Principles Underpinning the Performance of the Metal−Organic Framework HKUST-1. *Chem. Sci.* **2015**, *6*, 3674−83.
(38) Felthouse, T. R. The Chemistry, Structure, and Metal Metal-Bonding in Compounds of Rhodium(II). *Prog. Inorg. Chem.* **2007**, *29*, 73−166.
(39) Liu, J.; Wang, Y.; Benin, A. I.; Jakubczak, P.; Willis, R. R.; LeVan, M. D. CO_2/H_2O Adsorption Equilibrium and Rates on Metal−Organic Frameworks: HKUST-1 and Ni/DOBDC. *Langmuir* **2010**, *26*, 14301−7.
(40) Wang, Y. X.; Zhao, M. T.; Ping, J. F.; Chen, B.; Cao, X. H.; Huang, Y.; Tan, C. L.; Ma, Q. L.; Wu, S. X.; Yu, Y. F.; Lu, Q. P.; Chen, J. Z.; Zhao, W.; Ying, Y. B.; Zhang, H. Bioinspired Design of Ultrathin 2D Bimetallic Metal−Organic-Framework Nanosheets Used as Biomimetic Enzymes. *Adv. Mater.* **2016**, *28*, 4149−55.
(41) Nickerl, G.; Stoeck, U.; Burkhardt, U.; Senkovska, I.; Kaskel, S. A Catalytically Active Porous Coordination Polymer Based on a Dinuclear Rhodium Paddle-Wheel Unit. *J. Mater. Chem. A* **2014**, *2*, 144−8.
(42) Perdew, J. P.; Burke, K.; Ernzerhof, M. Generalized Gradient Approximation Made Simple. *Phys. Rev. Lett.* **1996**, *77*, 3865−8.
(43) Slater, J. C.; Johnson, K. H. Self-Consistent-Field Chi Alpha Cluster Method for Polyatomic-Molecules and Solids. *Phys. Rev. B* **1972**, *5*, 844.
(44) Lee, C. T.; Yang, W. T.; Parr, R. G. Development of the Colle-Salvetti Correlation-Energy Formula into A Functional of the Electron-Density. *Phys. Rev. B: Condens. Matter Mater. Phys.* **1988**, *37*, 785−9.
(45) Becke, A. D. Density-Functional Thermochemistry 0.3. The Role of Exact Exchange. *J. Chem. Phys.* **1993**, *98*, 5648−52.
(46) Gulde, R.; Pollak, P.; Weigend, F. Error-Balanced Segmented Contracted Basis Sets of Double-Zeta to Quadruple-Zeta Valence Quality for the Lanthanides. *J. Chem. Theory Comput.* **2012**, *8*, 4062−8.
(47) Grimme, S.; Antony, J.; Ehrlich, S.; Krieg, H. A Consistent and Accurate Ab Initio Parametrization of Density Functional Dispersion Correction (DFT-D) for the 94 Elements H-Pu. *J. Chem. Phys.* **2010**, *132*, 154104.
(48) Becke, A. D.; Johnson, E. R. A Density-Functional Model of the Dispersion Interaction. *J. Chem. Phys.* **2005**, *123*, 154101.
(49) Johnson, E. R.; Becke, A. D. A Post-Hartree−Fock Model of Intermolecular Interactions: Inclusion of Higher-Order Corrections. *J. Chem. Phys.* **2006**, *124*, 174104.
(50) Johnson, E. R.; Becke, A. D. A Post-Hartree−Fock Model of Intermolecular Interactions. *J. Chem. Phys.* **2005**, *123*, 024101.
(51) Kalinowski, J.; Wennmohs, F.; Neese, F. Arbitrary Angular Momentum Electron Repulsion Integrals with Graphical Processing Units: Application to the Resolution of Identity Hartree−Fock Method. *J. Chem. Theory Comput.* **2017**, *13*, 3160−70.

https://dx.doi.org/10.1021/acs.jpclett.0c02539
J. Phys. Chem. Lett. 2020, 11, 8138−8144

(52) Kesharwani, M. K.; Brauer, B.; Martin, J. M. L. Frequency and Zero-Point Vibrational Energy Scale Factors for Double-Hybrid Density Functionals (and Other Selected Methods): Can Anharmonic Force Fields Be Avoided? *J. Phys. Chem. A* **2015**, *119*, 1701−14.
(53) Yanai, T.; Tew, D. P.; Handy, N. C. A New Hybrid Exchange-Correlation Functional Using the Coulomb-Attenuating Method (CAM-B3LYP). *Chem. Phys. Lett.* **2004**, *393*, 51−7.

https://dx.doi.org/10.1021/acs.jpclett.0c02539
J. Phys. Chem. Lett. 2020, 11, 8138−8144